vese turns in the α helices discussed above. The reverse turns and loops in the proteins are generally exposed to the aqueous environment and are highly hydrated. Our preliminary analysis of the patterns of hydration of these loops and turns indicates that the water molecules again play an intimate role in directing the chain folding (*17*) and thus probably play a key role in driving protein folding.

REFERENCES AND NOTES

1. C. B. Anfinsen, *Science* **181**, 223 (1973).
2. P. E. Wright, H. J. Dyson, R. A. Lerner, *Biochemistry* **27**, 7167 (1988).
3. C. L. Tsou, *ibid.*, p. 1809.
4. C. M. Venkatachalam, *Biopolymers* **6**, 1425 (1968).
5. C. Ramakrishnan and G. N. Ramachandran, *Biophys. J.* **5**, 909 (1965).
6. K. A. Satyshur *et al.*, *J. Biol. Chem.* **263**, 1628 (1988), and unpublished results. The large difference in the interhelical angles of the apo calcium-binding motifs (AB 139° and CD 149°) probably stems from the B helix being kinked by the presence of inserted water molecules. In contrast, the interhelical angles of the holo calcium-binding motifs (EF 113° and GH 113°) are the same.
7. I. L. Karle, J. Flippen-Anderson, K. Uma, P. Balaram, *Proc. Natl. Acad. Sci. U.S.A.* **85**, 299 (1988).
8. F. C. Bernstein *et al.*, *J. Mol. Biol.* **112**, 535 (1977).
9. G. A. Jeffrey and J. Mitra, *J. Am. Chem. Soc.* **106**, 5546 (1984); G. A. Jeffrey, in *Landolt-Bornstein*, vol. VII/1, *Nucleic Acids*, W. Saenger, Ed. (Springer Verlag, Berlin, in press); U. C. Singh and P. A. Kollman, *J. Chem. Phys.* **83**, 4033 (1985).
10. T. L. Blundell, D. J. Barlow, N. Borkakoti, J. M. Thornton, *Nature* **306**, 281 (1983).
11. J. L. Crawford, W. N. Lipscomb, C. G. Schellman, *Proc. Natl. Acad. Sci. U.S.A.* **70**, 538 (1973).
12. The amino acid composition (in %) derived from the 26 inserted segments is: A, 16.15; G, 11.54; L, 5.38; I, 5.38; V, 3.08; F, 2.31; Y, 2.31; W, 0.77; P, 0.77; S, 6.92; T, 4.62; C, 2.31; M, 3.85; E, 6.92; D, 6.92; K, 8.46; R, 2.31; H, 3.85; O, 2.31; and N, 3.85. Abbreviations for the amino acid residues are: A, Ala; C, Cys; D, Asp; E, Glu; F, Phe; G, Gly; H, His; I, Ile; K, Lys; L, Leu; M, Met; N, Asn; P, Pro; Q, Gln; R, Arg; S, Ser; T, Thr; V, Val; W, Trp; and Y, Tyr. 3BCL with three inserted segments, which has only the x-ray sequence, and 3CTS with four inserted segments, whose sequence is unknown, were not included in calculation. Of the total of 130 residues in the 26 segments, Ala occurred 21 times and Gly 15 times. Composition of Ala and Gly in the inserted segments exceeded that of α helix middle by 3 and 6.5%, respectively.
13. The amino acid composition of the helix termini and the helix middle were extracted from P. Y. Chou and G. E. Fasman [*Adv. Enzymol.* **47**, 45 (1978)]. The helix termini include the three residues in either side of the helix boundaries and the α-helix middle excludes the three residues at the helix ends. The correlation coefficients given in the text were calculated using the relation $(Y_{est} = \overline{Y}_{est})^2/(Y = \overline{Y})^2$, where Y represents the amino composition of the inserted segments and Y_{est} represents the expected composition for the helix middles or reverse turns.
14. H. J. Dyson, M. Rance, R. A. Houghten, P. E. Wright, R. A. Lerner, *J. Mol. Biol.* **201**, 201 (1988). These authors (*ibid.*, p. 161) have also shown the presence of type-II and type-VI reverse turns in aqueous solution of a series of synthetic penta- and hexapeptide segments containing Pro and Gly by ^{1}H nuclear magnetic resonance studies. This result was expected for such sequences but was initially observed in solution by these workers. We find that water-inserted α-helical segments do not favor the type-VI reverse turn.
15. S. S. Zimmerman and H. A. Scheraga, *Proc. Natl. Acad. Sci. U.S.A.* **74**, 4126 (1977).
16. P. S. Kim and R. L. Baldwin, *Annu. Rev. Biochem.* **51**, 459 (1982).
17. M. Sundaralingam and Y. C. Sekharudu, unpublished results.

18. Supported by NIH grant AR-34139, the College of Agricultural and Life Sciences, and the University Graduate School. We dedicate this paper to G. A. Jeffrey, professor emeritus, Department of Crystallography, University of Pittsburgh.

7 December 1988; accepted 21 March 1989

Global Positioning System Measurements for Crustal Deformation: Precision and Accuracy

WILLIAM H. PRESCOTT, JAMES L. DAVIS, JERRY L. SVARC

Analysis of 27 repeated observations of Global Positioning System (GPS) position-difference vectors, up to 11 kilometers in length, indicates that the standard deviation of the measurements is 4 millimeters for the north component, 6 millimeters for the east component, and 10 to 20 millimeters for the vertical component. The uncertainty grows slowly with increasing vector length. At 225 kilometers, the standard deviation of the measurement is 6, 11, and 40 millimeters for the north, east, and up components, respectively. Measurements with GPS and Geodolite, an electromagnetic distance-measuring system, over distances of 10 to 40 kilometers agree within 0.2 part per million. Measurements with GPS and very long baseline interferometry of the 225-kilometer vector agree within 0.05 part per million.

RELATIVE MOTION OF THE MAJOR tectonic plates of the earth produces crustal deformation along the plate margins. This deformation typically involves strain rates of 0.1 to 0.5 ppm/year (*1*). Since late in the 19th century [for example, (*2*)], our understanding of crustal deformation has benefitted greatly from geodetic observations. Until recently, studies of the deformation occurring in plate boundary zones relied on data from triangulation, trilateration, and leveling. However, GPS surveying is rapidly becoming the preferred technique. In addition to providing a great deal of flexibility in selection of stations and a greater tolerance for adverse weather conditions and air quality than the older techniques, GPS provides a direct observation of three translation components and orientation. With land-based surveying, techniques must be combined in order to obtain all three translation components of station motion and the precision of the determination of the rotational part of the deformation is far below that of the other components. The ability to observe directly all translational components plus orientation between stations separated by any distance allows us to study plate deformation at broad scales over hundreds of kilometers as well as within a few meters in fault zones. Since late 1985, we have made repeated GPS measurements of the relative positions of stations in the western United States. In this report, we use this data set to examine the repeatability of GPS vectors and to compare GPS measurements with those from other techniques.

The heart of GPS is a set of satellites (currently 7 active, but eventually 21) orbiting the earth at an altitude of approximately 20,000 km. These satellites transmit on two L-band frequencies, L_1 at 1575.42 MHz and L_2 at 1227.60 MHz. Receivers record time-tagged pseudo-range and phase observations (*3*) from L_1, L_2, or both. The signals broadcast by the satellites allow the user to determine the location of a single receiver with an accuracy of a few meters. For geodetic applications, at least two receivers are required. The satellite signals are then used in differential processing to determine the relative position of the receivers with an uncertainty 10^{-3} times as small as the measurement obtained with a single receiver.

The largest number of repeated observations are measurements of the relative positions of four stations in the vicinity of Parkfield, California (Fig. 1). Estimates of relative position were obtained from monthly GPS measurements (*4–10*), the series extending from January 1986 to October 1988. In all of the solutions, the coordinates of station 10JDG were fixed (*11*), and coordinates of the other three stations relative to station 10JDG were determined for each set of observations. The secular trends in station movement (Fig. 2) indicate that there was significant motion only in the component of velocity parallel to the strike of the San Andreas fault (Table 1). Rates obtained with GPS are consistent with other estimates of the creep rate (*12*) in the Parkfield area. The vertical component of one observation for station Joaquin is a clear outlier. We suspect that there was an error in the measurement of the antenna height.

The variations about the best fitting straight line are of particular interest for assessing the precision of the observations

U. S. Geological Survey, 345 Middlefield Road, Mail Stop 977, Menlo Park, CA 94025.

Fig. 1. Map of the western United States showing detail of all the stations.

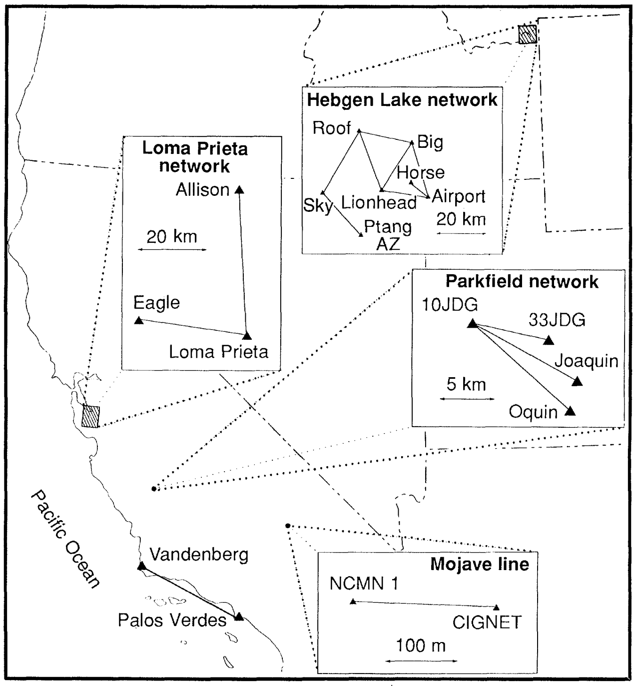

(Table 2). For a long series, a nonlinear component of tectonic deformation may be interpreted as part of the noise, resulting in a root mean square (rms) that is an overestimate of the errors. With a short series, the entire spectrum of errors may not be sampled, resulting in a rms that may be an underestimate. We chose a conservative approach and used the longest possible time span in calculating the rms; in most cases the data spanned more than a year. The values in Table 2 are our best estimate of the current repeatibility of GPS.

We have analyzed data for several experiments besides Parkfield (Table 2 and Fig. 1), including measurements of the CIGNET–NCNM 1 line, a 242-m vector from the GPS fiducial station at Mojave, California, to a reference mark nearby, two vectors at Loma Prieta, a vector from Palos Verdes to Vandenberg, and several vectors at Hebgen Lake, Montana. The two Loma Prieta vectors have the shortest observation span with just 10 months from the first observation to the last. The data from these experiments suggest that the errors do not grow monotonically with increasing line length. Both the north and east components of the Palos Verdes to Vandenberg vector have smaller errors than the corresponding components of the much shorter Loma Prieta lines. This effect may be attributed to differences in the observing strategy used in each experiment: receivers at Palos Verdes and Vandenberg tracked satellites 8 hours per day for 3 to 4 days during each experiment, whereas at Loma Prieta each observation consisted of 5 hours of tracking on a single day.

Table 1. Velocities and standard deviations of Parkfield stations relative to 10JDG in a fault-oriented coordinate system derived from data in Fig. 2.

Station	Parallel* (mm/year)	Normal† (mm/year)
33JDG	11.9 ± 0.9	−1.1 ± 1.0
Joaquin	9.0 ± 1.0	1.9 ± 1.1
Oquin	−2.4 ± 1.1	0.1 ± 1.0

*The positive direction is azimuth 140°, approximately parallel to the San Andreas fault. †The positive direction is 230°, approximately normal to the San Andreas fault.

The Parkfield, Loma Prieta, and Palos Verdes to Vandenberg vectors have been measured by techniques other than GPS. The length of the Loma Prieta vectors have been measured nearly 100 times since 1981 with a Geodolite, an electromagnetic distance-measuring system (*13*). The difference between the mean of the GPS observations and the Geodolite observations for the same time period is 9.7 ± 4 mm (0.22 ± 0.09 ppm) for the Allison line and 0.4 ± 4 mm (0.01 ± 0.13 ppm) for the Eagle line (Fig. 3). The Geodolite and GPS length measurements both depend on the value used for the velocity of light in a vacuum. The velocity used in processing the Geodolite observations was adopted in 1970 and differs by 0.14 ppm from the current value used in GPS processing. In comparing GPS and Geodolite, we corrected the Geodolite observations to make them consistent with the more modern velocity. A second complication with the Geodolite-GPS comparison is that, because of differing visibility requirements, different stations were used by the

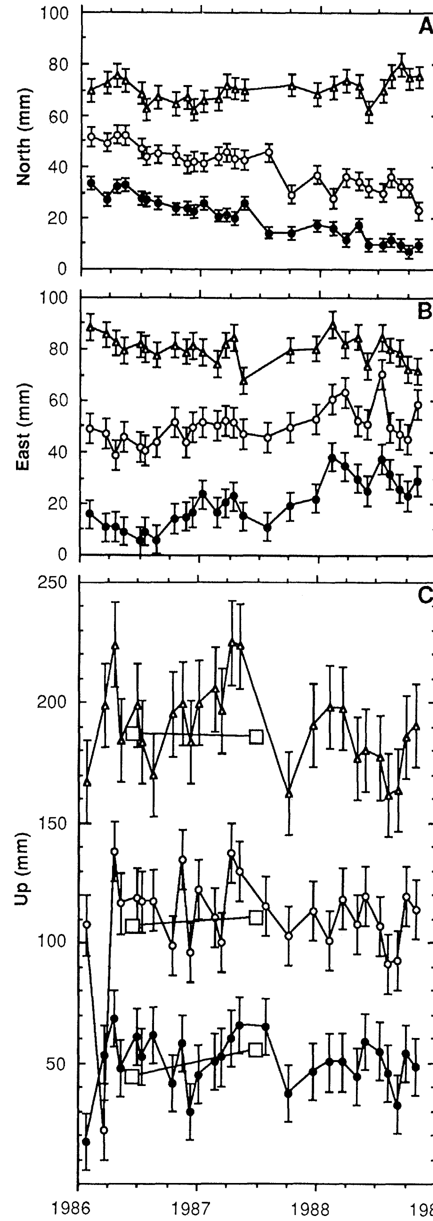

Fig. 2. Plots of the (**A**) north, (**B**) east, and (**C**) vertical (up) components of the Parkfield vectors as a function of time. Solid circles represent data for station 33JDG, open circles data for Joaquin, and open triangles data for Oquin. Error bars for all GPS data come from the misfit to a linear trend (Table 2). The large open squares on the plot of the vertical component (C) are derived from leveling data (*14*).

two systems. We have corrected for the offset, but it introduces an additional uncertainty in the comparison.

A comparison that is not subject to eccentric-station complications is afforded by eight lines near Hebgen Lake, Montana. These lines were measured with both Geodolite and GPS in August and September 1987. The mean difference between Geodolite and GPS for all ten comparisons, eight from Hebgen and two from Loma Prieta, is 1.1 ± 2.6 mm (Fig. 4). Consequently, the

Table 2. Summary of the estimates of precision of GPS observations from root-mean-square (rms) residuals; *N*, number of observations. The rms was calculated from the residuals to the best-fitting straight line to all of the data.

Station 1	Station 2	*N*	Time span (months)	Vector length (km)	North rms (mm)	East rms (mm)	Up rms (mm)	Length rms (mm)
CIGNET	NCNM1	4	20	0.24	1.5	1.8	4.6	1.4
10JDG	33JDG	27	34	7.0	2.5	5.6	11.8	5.4
10JDG	Joaquin	27	34	10.6	3.6	5.8	12.5*	5.9
10JDG	Oquin	26	34	11.9	4.4	5.0	17.4	4.4
Loma Prieta	Eagle	7	10	31.4	10.7	9.8	17.6	9.1
Loma Prieta	Allison	8	10	43.2	11.5	17.7	21.3	10.8
Palos Verdes	Vandenberg	6	24	223.1	6.1	10.9	38.8	10.8

*One discrepant outlier in this series was omitted in calculating the rms.

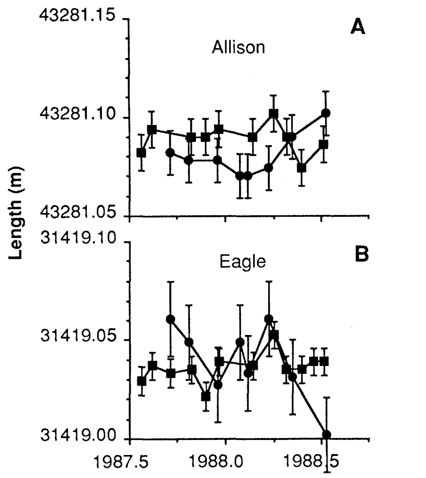

Fig. 3. Geodolite (squares) and GPS (circles) data for two lines observed with both systems; (**A**) data for the Loma Prieta–Allison line; (**B**) Loma Prieta–Eagle line. Error bars for Geodolite come from (*13*) and for GPS from Table 2.

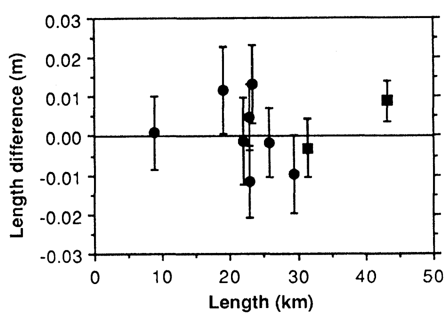

Fig. 4. Difference between Geodolite and GPS observations. Circles are differences of one Geodolite and one GPS observation of the same line at Hebgen Lake, Montana. Squares are differences of the the means of data shown in Fig. 3. Error bars are computed from (*13*) and Table 2.

data suggest that there is no significant difference between the two systems at the level of 0.2 ppm.

The four stations of the Parkfield network are part of a line that is leveled to first-order standards annually (*14*). The elevation differences obtained from the leveling (Fig. 2) are well within the scatter in the GPS observations. Because we are considering only changes of elevation difference, the distinction between orthometric and ellipsoidal heights is irrelevant. In addition to the two leveling observations that are contemporaneous with the GPS measurements, there are two earlier level surveys. The rms of all four level surveys is 4.4 mm for station pair 10JDG-33JDG, 5.2 mm for 10JDG-Joaquin, and 4.8 mm for 10JDG-Oquin. These values are significantly smaller than the GPS measurements of 11.8 mm, 12.5 mm, and 17.4 mm of the vertical component for the same sites (Table 2). At these distances, relative elevation is determined more precisely with conventional leveling. At longer distances, GPS might provide the more precise measurement because GPS errors appear to grow more slowly with distance than leveling errors [Table 2 and (*15*)].

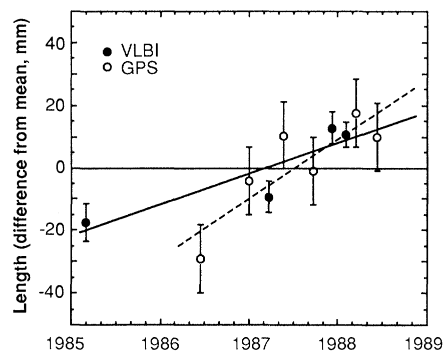

Fig. 5. Length of Palos Verdes–Vandenberg line measured by VLBI (solid circles) and by GPS (open circles); GPS error bars are from Table 2; VLBI error bars were calculated by propagation of error estimates through the solution.

The Palos Verdes to Vandenberg line has been observed by very long baseline interferometry (VLBI) four times in the past few years. On the basis of a comparison of GPS and VLBI measurements (Fig. 5), there is no significant offset between the two measurements over this >200-km line. The two techniques appear to indicate that there is a different rate of lengthening along this line, but, given the small sample size, this difference is not significant.

At its present level of precision, GPS provides a useful signal-to-noise ratio for monitoring plate motion and plate margin deformation at scales from 10 m to at least 200 km over periods of a few years. In order to achieve this precision, it is necessary to have clean, high-quality data from a network of tracking stations and careful (time-consuming) data processing to improve orbits. For lines less than about 10 km, the current broadcast orbits are adequate, and obtaining high precision is then somewhat less time-consuming.

REFERENCES AND NOTES

1. 0.1 ppm/year = 0.3 × 10^{-14}/s; W. H. Prescott, J. C. Savage, W. T. Kinoshita, *J. Geophys. Res.* **84**, 5423 (1979).
2. H. F. Reid, in *The California Earthquake of April 18, 1906, Report of the State Earthquake Investigation Commission* (Carnegie Institution of Washington, Washington, DC, 1910), vol. 2, pp. 16–28.
3. J. J. Spilker, *Navigation* **25**, 122 (1980).
4. The data were collected with dual-frequency TI-4100 receivers. Each observation session consisted of 4 to 8 hours of satellite tracking. Air pressure, temperature, and humidity near the station were recorded approximately once every hour; GESAR software (*5*) was used to control the receivers and to record data. The processing was done with Bernese version 3.0 software (*6*). In addition to solving for any subset of the station coordinates, we also solved for orbital elements (*7*) for each satellite, atmospheric zenith-delay parameters, ionospheric model coefficients, and cycle ambiguity terms (*8*). For short vectors (12 km or less), our results include only L_1 processing (*9*) with broadcast satellite ephemerides. Cycle-count ambiguities were first estimated, then set to integers and removed from the solution. For longer vectors, it was necessary to estimate satellite orbit parameters as well as station coordinates, because the orbits become a primary source of error at longer distances. Thus, the data from stations in the local networks were supplemented with all available simultaneous data from a network of fiducial stations in North America (*10*), and orbit parameters were adjusted as part of the solution. In modeling the satellite orbits, we used arcs of several days, even if the local observations were made during a single day. For longer vectors, the difference between the L_1 and L_2 phase observations was used to estimate and to remove the ionospheric delay, creating the so-called ionosphere-free observable (*8*); satellite cycle ambiguities were estimated and not fixed to integers.
5. R. Darnell and L. Hawkins, *User's Guide to GESAR Version 1.0* (Applied Research Laboratory, University of Texas, Austin, 1986).
6. W. Gurtner, G. Beutler, I. Bauersima, T. Schildknecht, in *Proceedings of the First International Symposium on Precise Positioning with the Global Positioning System*, Rockville, MD, 15 to 19 April 1985 (National Geodetic Information Center, Rockville, MD, 1985), vol. 1, p. 363.
7. G. Beutler, W. Gurtner, I. Bauersima, R. Langley, *ibid.*, p. 99. We have made a few modifications to the algorithms and implemented the software on Macintosh microcomputers.
8. R. W. King, E. G. Masters, C. Rizos, A. Stolz, J. Collins, *School of Surveying Monogr. 9* (University of New South Wales, Kensington, Australia, 1985).
9. On these short vectors, much of the difference between L_1 and L_2 is random. Neglecting the ionospheric correction reduces the scatter at the expense of introducing a bias (0.3 to 0.5 ppm, or 2 to 6 mm, for the three vectors at Parkfield); a similar bias of about 0.5 ppm was found by Y. Georgiadou and A. Kleusberg [*Manusc. Geodaet.* **13**, 1 (1988)].

There is no definitive statement of the precision of the broadcast ephemerides. Our experience suggests that they are accurate at about the 5-m level, or ~0.25 ppm. We obtained the same results (at the millimeter level) when we processed selected Parkfield observations with improved orbits.
10. M. Chin, *GPS Bull.* 1, 1 (1988).
11. We used a coordinate system derived from VLBI and satellite laser ranging coordinates [M. Murray and R. King, *Mass. Inst. Tech. Intern. Memo.* (11 March 1988)]. The coordinates of station 10JDG in this system were determined from GPS observations to the VLBI station Fort Ord.
12. S. S. Schulz *et al.*, *J. Geophys. Res.* 87, 6977 (1982). Because the creep rate varies along strike in this area, some interpolation is required in comparing the rates of instruments that are not collocated.
13. J. C. Savage and W. H. Prescott, *ibid.* 78, 6977 (1973).
14. The leveling data were provided by R. Stein, personal communication.
15. R. S. Stein, *Earthquake Prediction* (*Maurice Ewing Ser. Monogr. 4*, American Geophysical Union, Washington, DC 1984).
16. The authors thank E. Himwich for providing the VLBI solutions. Part of this work was done while J.L.D. held a National Research Council–U.S. Geological Survey Research associateship.

27 January 1989; accepted 28 April 1989

Novel Sites of Expression of Functional Angiotensin II Receptors in the Late Gestation Fetus

MONICA A. MILLAN, PILAR CARVALLO, SHUN-ICHIRO IZUMI, SHARON ZEMEL, KEVIN J. CATT, GRETI AGUILERA

In the adult, the peptide hormone angiotensin II (AII) is primarily known as a regulator of circulatory homeostasis, but recent evidence also suggests a role in cell growth. This study of AII in late gestation rat fetuses revealed the unexpected presence of receptors in skeletal muscle and connective tissue, in addition to those in recognized adult target tissues. The AII receptors in this novel location decreased by 80 percent 1 day after birth and were almost undetectable in the adult. Studies in fetal skin fibroblasts showed that the receptors were coupled to phospholipid breakdown, with concomitant increases in inositol phosphate and cytosolic calcium. The abundance, timing of expression, and unique localization of functional AII receptors in the fetus suggest a role for AII in fetal development.

EMBRYOGENESIS, FETAL DEVELOPMENT, and growth are controlled by the coordinated action of a number of humoral regulators. In addition to traditional growth factors (*1*), an increasing number of peptide hormones have been implicated in cellular growth regulation (*2*). The octapeptide angiotensin II (AII), classically associated with control of blood pressure and electrolyte metabolism (*3*), stimulates cell growth and increases the expression of platelet-derived growth factor (PDGF) and the growth-related proto-oncogenes c-*myc* and c-*fos* in cultured smooth muscle cells (*4, 5*). Abundant binding sites for AII are present in membranes prepared from eviscerated rodent fetuses, indicating the presence of AII receptors at sites other than the traditional target in the adult (*6*). All components of the renin-angiotensin system, including immunoactive and bioactive AII, are found in the fetal-placental unit, thus providing the specific ligand for the fetal AII binding sites (*7*).

To characterize the topographic distribution of AII receptors in the fetus, we obtained female Sprague-Dawley rats at 7 to 21 days of gestation, litters of different ages, and adults from Zivic Miller (Zelienople, PA). Rats were killed and fetuses were immediately removed and frozen at −40°C. Autoradiographic analysis of AII receptors in the fetuses was performed by binding of ^{125}I-labeled [Sar^1,Ile^8]AII to slide-mounted sections (*8*).

Midsagittal and lateral sagittal autoradiograms from a 19-day-old fetus are shown in Fig. 1, A and B, respectively. All organs are fully formed at this stage, and AII binding was readily detectable in known target tissues including the adrenal zona glomerulosa and medulla, kidney, liver, and smooth muscle of the bronchi, blood vessels, and gastrointestinal tract. Particularly striking, however, is the intense AII binding in areas not normally expected to contain AII receptors, such as the subepidermal layer of the skin, mesenchymal and connective tissues, and skeletal muscle, especially the tongue. Little or no binding was detectable by autoradiography in brain, spinal cord, cartilage, bone, fat, and heart. The observed binding was specific, since all staining was abolished by incubation in the presence of 1 μM unlabeled AII, but was unchanged by excess amounts of the unrelated peptides, corticotropin-releasing factor (CRF), arginine vasopressin (AVP), and adrenocorticotropic hormone (ACTH).

AII binding was first detected at about day 12, and by the time organogenesis was completed (day 15), its localization and density was as described in Fig. 1. The high receptor density seen by autoradiography

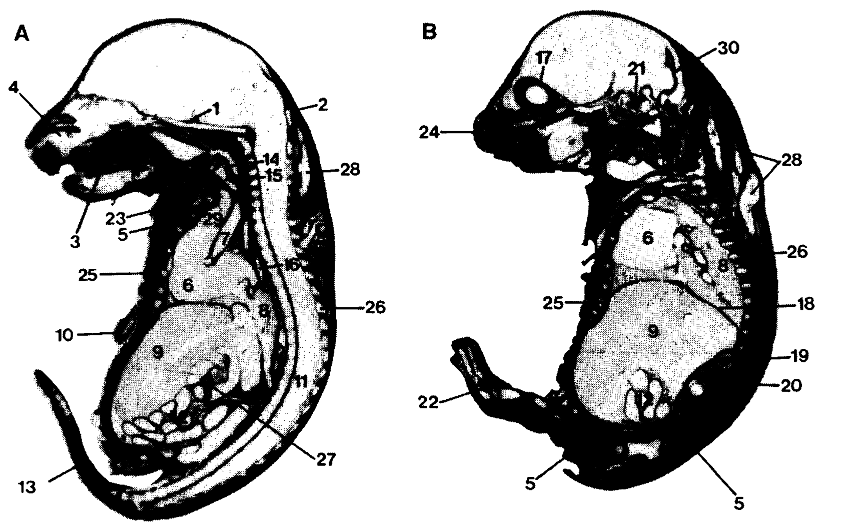

Fig. 1. Autoradiographic analysis of ^{125}I-labeled [Sar^1,Ile^8]AII binding to 20 μm of sagittal frozen sections of 19-day-old rat fetus (**A**) medial section (**B**) lateral section. Nonspecific binding measured in the presence of 1 μM AII was undetectable (not shown). Topographic distribution of the binding as determined by light microscopic analysis of the sections is indicated by the numbers: 1, pituitary gland; 2, mesenchymal tissue; 3, tongue; 4, nasal cavity; 5, skeletal muscle; 6, heart; 7, aorta; 8, lung; 9, liver; 10, umbilical cord; 11, spinal cord; 12, small bowel; 13, tail; 14, esophagus; 14, larynx; 16, trachea; 17, soft tissue around the eye; 18, diaphragm; 19, adrenal gland; 20, kidney; 21, inner ear; 22, hind foot; 23, salivary gland; 24, analgene of vibrissae; 25, rib; 26, vertebral bodies; 27, root of mesentery; 28, brown fat deposit; 29, thymus; and 30, meninges. The figure is representative of five similar experiments.

Section on Endocrine Physiology, Endocrinology and Reproduction Research Branch, National Institute of Child Health and Human Development, National Institutes of Health, Bethesda, MD 20892.